

Generic rigidity and accidental modes in metal-organic frameworks

Christopher M. Owen

*Department of Physics, Applied Physics, and Astronomy,
Binghamton University, Binghamton, NY 13902*

Michael J. Lawler

*Department of Physics, Applied Physics, and Astronomy,
Binghamton University, Binghamton, NY 13902 and
Department of Physics, Cornell University, Ithaca, NY 14853*

(Dated: December 2, 2025)

Metal-organic frameworks (MOFs) combine high porosity with structural fragility, raising important questions about their mechanical stability. We develop a rigidity-based framework in which spring networks parameterized by UFF4MOF are used to construct rigidity and dynamical matrices. Large-scale analysis of 5,682 MOFs from the CoRE 2019 database shows that most frameworks are formally over-constrained yet cluster sharply near the isostatic threshold, revealing accidental geometric modes and placing many MOFs near mechanical instability. In the representative case of UiO-66, we show that auxiliary long-range constraints introduced by tuning the neighbor cutoff lift these modes into soft, flat, finite-frequency bands. The results show that rigidity-matrix analysis can rapidly identify MOFs likely to remain mechanically stable. This near-criticality mirrors behavior known from topological mechanics and points to a deeper design principle in porous crystals.

I. INTRODUCTION

Metal-organic frameworks (MOFs) combine crystalline order with exceptional porosity, creating vast internal surface areas and highly tunable architectures that are promising for applications ranging from gas storage to catalysis (Fig. 1) [1, 2]. These same attributes often place MOFs near the edge of mechanical [3] stability: frameworks collapse during activation, deform under modest pressure, or exhibit soft, collective motions that couple strongly to guests molecules [4]. Predicting which structures are robust and which are mechanically fragile remains a central challenge [5, 6] for design and screening. Early efforts to describe MOF mechanics include the hinge-truss model of Sarkisov [7], which showed that framework flexibility can often be anticipated from network topology. Marmier and Evans [8] subsequently carried out a more mathematical, group-theoretical analysis of MOF frameworks, demonstrating that simple scalar Maxwell-Calladine counts are unreliable for MOFs. Since self stress can obscure underlying mechanisms a more robust method is needed thus motivating a matrix-based approach.

First principles and classical approaches each address part of this problem. Density functional theory (DFT) captures bonding and elastic responses with high accuracy but is limited to small cells [9]. Classical force fields and machine learned interatomic potentials (MLIPs) [10–12] extend accessible scales and enable dynamics for larger systems, but remain too computationally expensive for high throughput screening and often yield descriptive metrics without revealing the structural degrees of freedom that govern rigidity.

We take a complementary route based on rigidity theory, also known as topological constraint theory (TCT) [13, 14]. In this framework, a structure's mechan-

ical response is governed by the balance between internal degrees of freedom and the independent constraints imposed by its bonding network. The key objects are zero modes which are motions that cost no energy and states of self stress, which are patterns of internal tension and compression that satisfy force balance. The Maxwell-Calladine [15, 16] relation,

$$\nu \equiv N_0 - N_{ss} = dN_s - N_c, \quad (1)$$

links these quantities to network connectivity. In molecular terms, dN_s is the total atomic degrees of freedom and N_c is the number of linear bond stretching and angular bond bending constraints; together they fix the number of zero modes (N_0) and states of self stress (N_{ss}).

This constraint-based approach offers three advantages that are hard to obtain together with other methods. It clarifies which motions are allowed by the network topology, scales to system sizes suitable for high-throughput screening, and helps distinguish mechanically robust frameworks from those prone to soft modes or collapse.

In this work, we operationalize this program for MOFs by building constraint-based Hamiltonians with linear and angular springs, assembling rigidity matrices for periodic crystals, computing their Maxwell-Calladine indices, and phonon dispersions. The resulting modes are then characterized using the Inverse Participation Ratio (IPR) to distinguish between localized and collective motions, which is crucial for identifying the origins of framework flexibility. Spring constants are assigned from UFF4MOF [17–19] parameters, and all analyses are performed in reciprocal space to resolve wave vector-dependent zero modes. Applied to 5,682 frameworks in the CoRE 2019 [20] dataset, this approach reveals that most MOFs occupy a mechanically marginal regime while only a smaller subset behaves as genuinely rigid frame-

works. In this way, the rigidity-matrix analysis complements first-principles benchmarks: DFT and MLIPs provide accuracy for selected targets, while the present approach provides scalable guidance and interpretable relations across thousands of candidates.

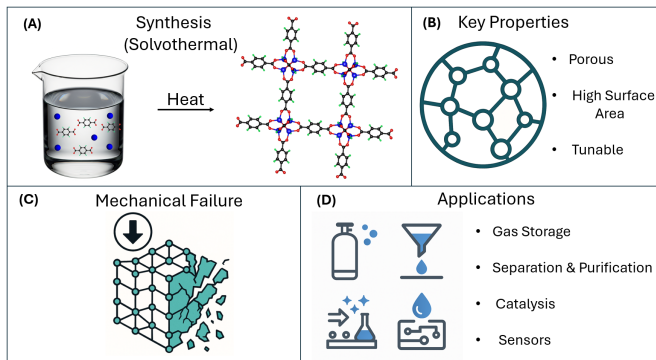


FIG. 1. **A:** MOFs are typically obtained via solvothermal methods [21], where metal ions or clusters and multidentate organic linkers self-assemble into extended crystalline networks. **B:** The resulting frameworks exhibit permanent porosity, high internal surface areas, and tunable structures and functionalities. **C:** Many MOFs are mechanically fragile and can degrade or collapse under external stress, highlighting the importance of identifying mechanically robust frameworks. **D:** MOFs have been investigated for gas storage, separations, heterogeneous catalysis, and chemical sensing.

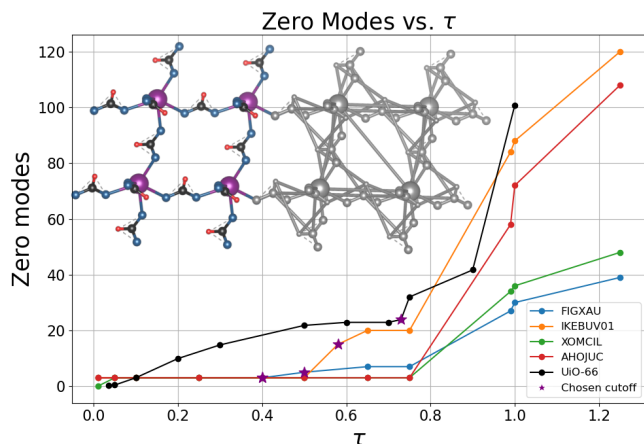


FIG. 2. Zero-mode count N_0 as a function of the constraint cutoff parameter τ , which controls which neighbors are included in the rigidity model. In our convention, larger τ reduces the coordination weight used by `CrystalNN`[22], removing constraints and increasing N_0 . Each colored curve corresponds to a different MOF, and purple stars (*) mark the plateau τ values selected automatically by `CrystalNN`. For clarity, the UiO-66 curve is scaled by a factor of 10. The inset shows the FIGXAU framework: Color indicates the baseline bonding network, while the gray version illustrates the auxiliary bonds identified when τ is reduced.

II. METHODOLOGY

A. Constraint-Based Model and Parameterization

We model each MOF as a periodic network of atoms connected by harmonic springs that penalize bond stretching and bond bending. The total Hamiltonian is

$$H = \sum_{i=1}^N \frac{p_i^2}{2m_i} + \frac{1}{2} \sum_{\mu} K_{\mu} (e_{\mu})^2 \quad (2)$$

where μ indexes all independent constraints in the network, including both bond-stretching terms $(i, j) \in \mathcal{L}$ and bond-bending terms $(i, j, k) \in \mathcal{A}$. The associated extensions are $e_{ij} = \hat{\mathbf{e}}_{ij} \cdot (\mathbf{u}_i - \mathbf{u}_j)$ and $e_{ijk} = \theta_{ijk} - \theta_{ijk}^0$. Stacking all extensions into a vector \mathbf{e} and displacements into \mathbf{u} defines the rigidity matrix R through $\mathbf{e} = R\mathbf{u}$. In our implementation, the same R used for Maxwell–Calladine counting also enters the energetic dynamical matrix once local stiffness and prestress are specified, consistent with the generalized rigidity analysis of Rocks and Mehta [23]. The potential energy and dynamical matrix then follow as:

$$V = \frac{1}{2} \mathbf{u}^T (R^T K R) \mathbf{u}, \quad D = M^{-1/2} R^T K R M^{-1/2} \quad (3)$$

Here M is the diagonal mass matrix constructed from the atomic masses m_i , and K_{μ} are the bond and angle spring constants obtained from UFF4MOF parameters, with atom types assigned according to local coordination environments. Explicitly,

$$K_{ij} = 664.12 \frac{Z_i Z_j}{r_{ij}^3}, \quad (4)$$

$$K_{ijk} = \frac{664.12}{r_{ij} r_{jk}} \frac{Z_i Z_k}{r_{ik}^5} \left[3 r_{ij} r_{jk} (1 - \cos^2 \theta_0) - r_{ik}^2 \cos \theta_0 \right], \quad (5)$$

where Z_{ℓ} are the UFF effective charges. We focus on these terms as they provide the dominant constraints governing framework rigidity. The UFF equilibrium distances are used as rest lengths; across all linear bonds they exceed the geometric bond lengths by 5–7% on average (see Appendix B).

The bonding network itself is determined using the `CrystalNN`[22] algorithm implemented in `pymatgen`[24]. A tunable cutoff parameter τ controls which coordination shells are included, as shown in Fig. 2. In the main dataset analysis we adopt the plateau τ identified by `CrystalNN`, which provides a chemically sensible minimal network, but in Fig. 4 we explore the effect of reducing τ for UiO-66, showing that modest additions of longer-range constraints systematically lift many of the baseline zero modes into soft, finite-frequency vibrations.

B. Phonon Dispersions and Localization Analysis

For periodic crystals, the model is solved in reciprocal space. Atomic displacements are expanded as plane

waves (see Appendix A),

$$\mathbf{u}_{m\alpha} = \frac{1}{\sqrt{N}} \sum_{\mathbf{k}} \mathbf{u}_{\alpha}(\mathbf{k}) e^{i\mathbf{k}\cdot\mathbf{R}_m},$$

which yields the \mathbf{k} -dependent dynamical matrix $D(\mathbf{k})$. Diagonalizing $D(\mathbf{k})$ gives the phonon spectrum $\omega^2(\mathbf{k})$, which we compute along the Setyawan–Curtarolo [25] high-symmetry paths in the Brillouin zone.

To distinguish between localized and delocalized vibrational modes, we calculate the inverse participation ratio (IPR). For a phonon mode at wavevector \mathbf{k} and band index j , the participation of atom i is $P_i(\mathbf{k}, j) = |\mathbf{u}_i(\mathbf{k}, j)|^2$. The IPR is then

$$\text{IPR}(\mathbf{k}, j) = \frac{\sum_{i=1}^N [P_i(\mathbf{k}, j)]^2}{\left(\sum_{i=1}^N P_i(\mathbf{k}, j)\right)^2} \quad (6)$$

Low IPR values (approaching $1/N$) indicate delocalized modes, whereas high values (approaching 1) signal localization. In degenerate subspaces we choose a random orthonormal basis, which provides a representative sampling of possible localization patterns.

C. Dataset and Implementation Details

We apply this framework to 5,682 structures from the CoRE MOF 2019 database [20]. Primitive cells are used whenever available to reduce redundancy. CIF [26] parsing, neighbor detection, constraint assembly, and phonon analysis were automated to enable large-scale screening. To validate our method, we benchmarked the rigidity code against crystalline silicon, shown in Appendix C, and against UiO–66, whose detailed analysis is presented in the main text. Full implementation details and all input files are provided in Appendix B and in the publicly available repository referenced therein.

III. RESULTS

Our large scale analysis of 5,682 CoRE MOF structures shows that most frameworks are formally over-constrained. As illustrated in Fig. 5, the distribution of the Maxwell–Calladine index ν is skewed toward negative values. However, rather than exhibiting a broad continuum of rigidity, these materials cluster sharply near the isostatic threshold $\nu = 3$.

This sharp concentration indicates a universal mechanical trend: the self-assembly of porous frameworks drives them toward the brink of mechanical instability. In our dataset, this marginal behavior dominated by *accidental geometric modes*, which are zero modes that do not appear in Maxwell–Calladine counting because the assumption of generic geometry is violated. The local geometry of the metal clusters and linkers creates alignments that render some constraints redundant, which leads to

accidental zero modes despite the large number of constraints. A smaller subset of truly generic frameworks, clustered around $\nu/N_s \approx -1.5$, display conventional stability. This confirms that accidental modes are a pervasive feature of MOF architectures rather than isolated anomalies.

To systematically characterize these behaviors, we classify frameworks into three regimes based on the relationship between ν and the vibrational spectrum:

- **Generic Rigidity** ($\nu < 3$, $N_0 = 3$): All constraints are independent. Topology dictates stability, and only global rigid-body zero modes occur.
- **Geometrically Unstable** ($\nu < 3$, $N_0 > 3$): Symmetry creates constraint redundancy, producing accidental nontrivial mechanisms despite being formally over constrained.
- **Singular Isostatic (accidental, $\nu = 3$)**: An accidental isostatic case in which internal zero modes and states of self stress coexist, with $N_0 > 3$, $N_{ss} > 0$, and $N_0 - N_{ss} = 3$.

Structures with $\nu > 3$ are classified as under-constrained and are stabilized only by weak long-range couplings. In practical terms, generically rigid frameworks are robust to small distortions, whereas geometrically unstable and singular isostatic frameworks can be pushed between rigid and soft behavior by modest geometric changes. To illustrate the physical implications of the three regimes, we examine the representative MOFs shown in Fig. 3.

ABIXOZ represents Generic Rigidity. It is strongly over-constrained with $\nu/N = -1.89$ and contains no zero modes. Its phonon dispersion in Fig. 3(A) is smooth and well ordered, and its IPR profile shows predominantly delocalized motion. ABIXOZ therefore serves as a reference for genuine topological rigidity in which the constraint count reliably predicts mechanical behavior.

IKEBUV01 exemplifies the Singular Isostatic regime. Residing at the mechanical critical point ($\nu = 3$), its stability is not generic but enforced by symmetry: it contains twelve zero modes exactly canceled by twelve states of self stress. Its phonon dispersion in Fig. 3(B) reveals low frequency asymmetries and nearly flat branches, signatures of marginal rigidity. The IPR map shows that many zero modes remain delocalized, but this balance is fragile; small geometric distortions could stabilize the system but the removal of periodic boundary conditions would likely drive the structure into a generically unstable phase.

UiO–66 lies within the Geometrically Unstable regime. Despite a Maxwell–Calladine index indicating high rigidity ($\nu/N = -1.14$), its spectrum contains 238 zero modes at Γ . These are accidental geometric modes arising from degeneracies within the MOF. The phonon dispersion in Fig. 3(C) shows bands that flatten near Γ , indicating internal degrees of freedom that permit compliant motion within an otherwise over-constrained network.

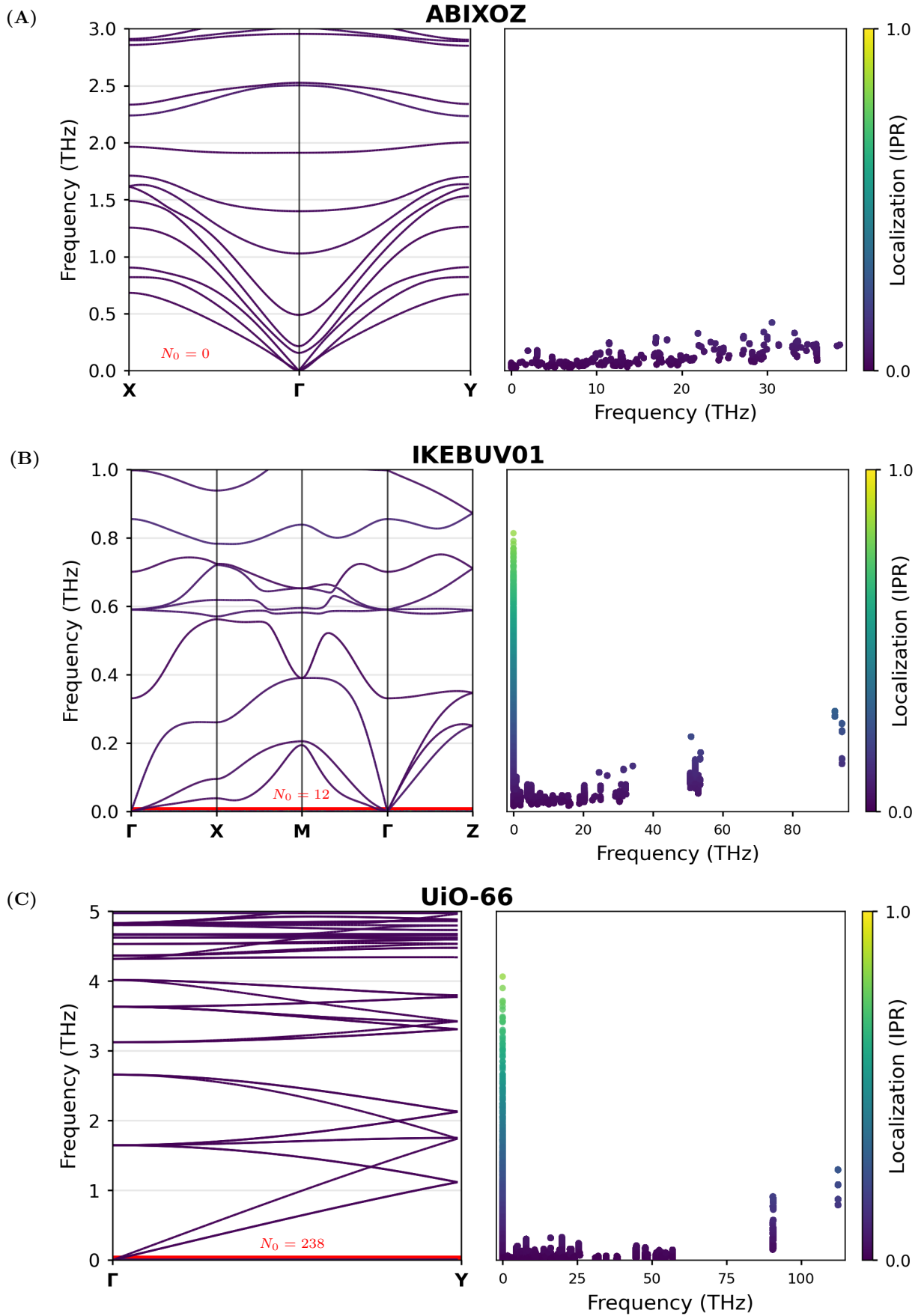


FIG. 3. Phonon dispersions and inverse participation ratio (IPR) maps for representative materials. (A) ABIXOZ ($\nu/N_s = -1.89$) stable and over-constrained; (B) IKEBUV01 ($\nu/N_s = +0.075$) near-isostatic with delocalized soft modes; (C) UiO-66 ($\nu/N_s = -1.14$) moderately over-constrained with mixed localization behavior.

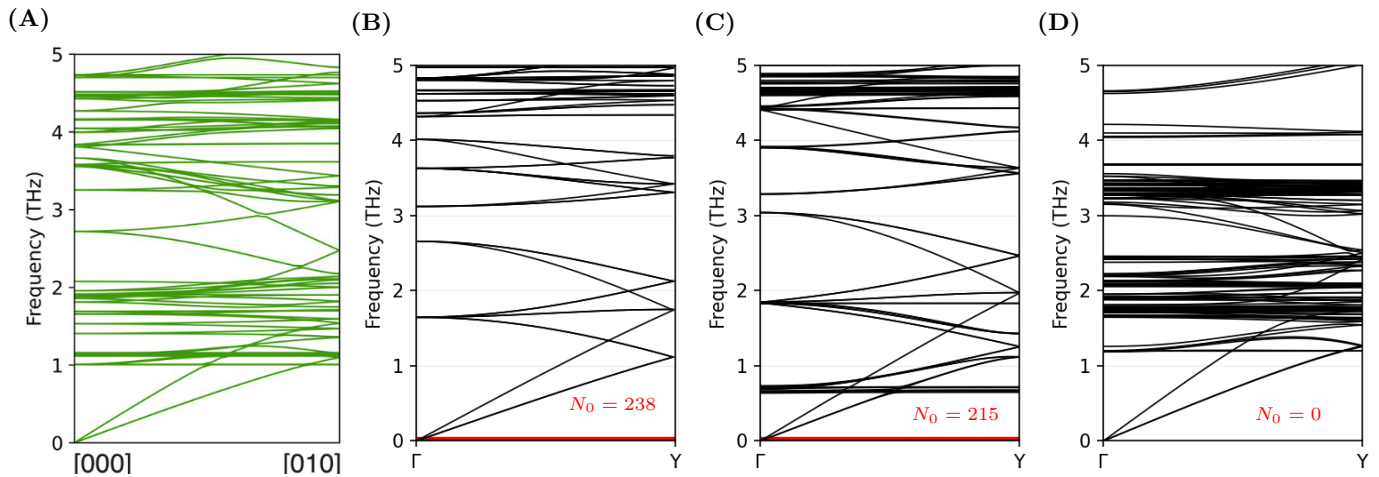


FIG. 4. (A) Benchmark phonon dispersion calculated via GULP, reproduced from Ref. [27]. (B) Corresponding result from our rigidity-based model ($N_0 = 238$) using the default τ setting. (C) Decreasing the cutoff to $\tau = 0.5$ introduces auxiliary constraints, reducing the zero mode count to $N_0 = 215$. (D) Further tuning to $\tau = 0.035$ eliminates all zero modes ($N_0 = 0$). The progression from (B) to (D) demonstrates how assigning finite stiffness to long-range auxiliary bonds lifts zero modes into soft, collective bands, progressively filling the low-frequency spectrum relative to the benchmark in (A).

To confirm the geometric origin of these modes, we systematically introduce auxiliary long-range bonds by tuning the cutoff parameter τ (Fig. 4). As τ decreases, the constraint density increases. By assigning finite stiffness to these auxiliary bonds while retaining standard UFF parameters for the primary network, we observe that the zero modes are lifted to finite frequencies, manifesting as soft, collective modes.

Taken together, these case studies show that formal constraint counting alone cannot predict rigidity in porous crystalline materials. While ABIXOZ behaves as a generic over-constrained network, UiO-66 and IKE-BUV01 derive their mechanical character from accidental geometric modes and constraint dependencies. Distinguishing between generic and accidental modes is therefore essential for understanding and predicting the mechanical stability of MOFs.

IV. DISCUSSION

Our results reveal that most MOFs occupy a mechanically marginal regime. Although the majority of frameworks are formally over-constrained, their node and linker geometries introduce *accidental geometric modes* that make some constraints effectively dependent. These additional zero modes either destabilize the MOF's structure or introduce soft cubic or quartic modes. Only a smaller subset of materials, such as ABIXOZ, exhibits fully independent constraints and behaves as a genuinely rigid and topologically stable network.

UiO-66, which is widely regarded as a stable MOF [28, 29], illustrates how geometric arrangement rather than insufficient coordination can produce internal soft modes. The accidental modes identified in the baseline

model arise from specific alignments within the Zr-O clusters and linker geometries that render certain constraints redundant. These motions correspond to internal flexibilities relevant to activation and guest molecule accommodation, yet they do not compromise the overall stability of the framework. When auxiliary long-range constraints are introduced by adding bonds that arise when decreasing τ , these accidental dependencies are removed, and the zero modes are lifted into low-frequency vibrational branches. This confirms that the soft motions originate from geometric degeneracy rather than from an actual deficit of constraints.

While the present rigidity-based analysis provides these mechanistic insights, it is subject to several approximations. The harmonic model captures only small amplitude motions, and quantitative accuracy depends on the UFF4MOF parameterization. The omission of nonbonded forces and entropic contributions limits the description of large deformations and finite temperature effects. Despite these simplifying assumptions, the correspondence with first-principles calculations for benchmark systems indicates that the model captures the essential degree of freedom structure that governs phonon modes.

Taken together, these results bridge the gap between simple topological metrics and fully atomistic simulations. Maxwell-based counting alone cannot predict mechanical stability in crystalline porous materials. Rigidity matrix analysis, however, determines whether geometric constraints are independent or redundant, allowing rapid identification of both genuinely rigid and potentially fragile structures. This capability establishes a scalable and interpretable foundation for mechanical screening across large materials databases.

Finally, the prevalence of near-isostatic frameworks re-

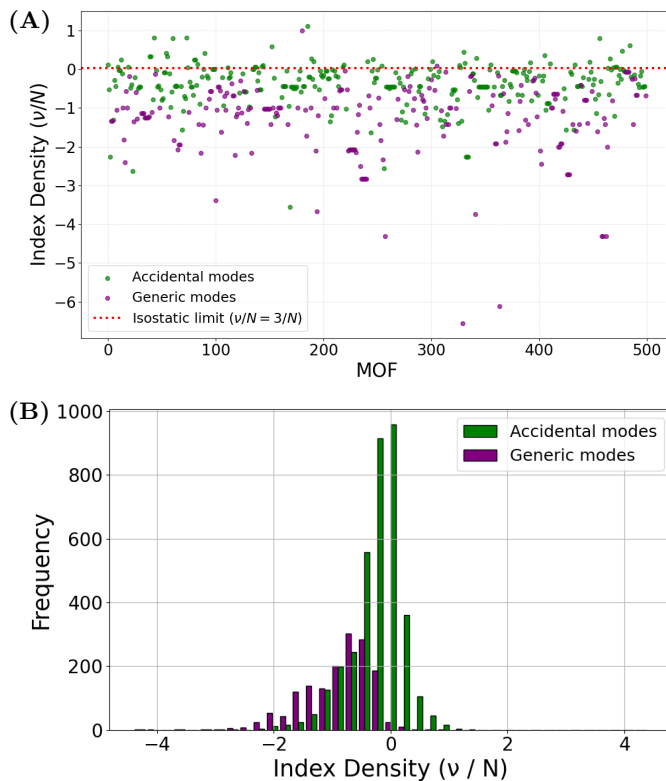


FIG. 5. Rigidity statistics across the CoRE MOF dataset. (A) Scatter plot of ν for 500 representative MOFs, with the red dashed line marking the isostatic threshold ($\nu = 3$). (B) Histogram of the Maxwell–Calladine index density (ν/N) for 5,182 MOFs at Γ . The majority of frameworks are formally over-constrained yet cluster sharply near the isostatic point. This concentration is dominated by accidental modes, which place many MOFs on the verge of mechanical instability.

vealed here points toward a broader connection between MOF mechanics and ideas from topological mechanics. The parallels to isostatic lattices explored by Kane and Lubensky [30] suggest that similar topological features, including protected boundary modes, may be realizable in complex porous crystals.

ACKNOWLEDGMENTS

This material is based upon work supported by the National Science Foundation under Grant No. DMR-1940243.

Appendix A: Fourier Transformed Rigidity Matrix

To analyze vibrational modes in periodic structures, we work in reciprocal space by Fourier transforming the atomic displacements. Each atom is indexed by its unit cell position \mathbf{R}_m and an internal label α identifying the atom within the cell. The displacement of atom (m, α)

is expanded as

$$\mathbf{u}_{m\alpha} = \frac{1}{\sqrt{N}} \sum_{\mathbf{k}} \mathbf{u}_{\alpha}(\mathbf{k}) e^{i\mathbf{k}\cdot\mathbf{R}_m}, \quad (\text{A1})$$

where N is the number of unit cells, \mathbf{k} runs over wave vectors in the first Brillouin zone, and $\mathbf{u}_{\alpha}(\mathbf{k})$ are the Fourier components of the displacements.

The bond extension for a linear constraint (spring) connecting atom (m, α) to atom (n, β) is

$$e_{\ell} = \hat{\mathbf{r}}_{m\alpha, n\beta} \cdot (\mathbf{u}_{m\alpha} - \mathbf{u}_{n\beta}), \quad (\text{A2})$$

where $\hat{\mathbf{r}}_{m\alpha, n\beta}$ is the unit vector along the bond. Substituting the Fourier representation gives

$$\begin{aligned} e_{\ell} &= \hat{\mathbf{r}}_{m\alpha, n\beta} \cdot \frac{1}{\sqrt{N}} \sum_{\mathbf{k}} [\mathbf{u}_{\alpha}(\mathbf{k}) e^{i\mathbf{k}\cdot\mathbf{R}_m} - \mathbf{u}_{\beta}(\mathbf{k}) e^{i\mathbf{k}\cdot\mathbf{R}_n}] \\ &= \frac{1}{\sqrt{N}} \sum_{\mathbf{k}} e^{i\mathbf{k}\cdot\mathbf{R}_m} \hat{\mathbf{r}}_{m\alpha, n\beta} \cdot [\mathbf{u}_{\alpha}(\mathbf{k}) - \mathbf{u}_{\beta}(\mathbf{k}) e^{i\mathbf{k}\cdot\boldsymbol{\delta}_{\ell}}], \end{aligned} \quad (\text{A3})$$

where $\boldsymbol{\delta}_{\ell} = \mathbf{R}_n - \mathbf{R}_m$ is the lattice vector difference between the two connected unit cells. Thus the bond extension at wave vector \mathbf{k} depends only on the displacements $\mathbf{u}_{\alpha}(\mathbf{k})$ and $\mathbf{u}_{\beta}(\mathbf{k})$ at the same \mathbf{k} .

Collecting all constraint extensions into a vector $\mathbf{e}(\mathbf{k})$ and the corresponding displacements into $\mathbf{u}(\mathbf{k})$, we define the Fourier transformed rigidity matrix $\mathbf{R}(\mathbf{k})$ by

$$\mathbf{e}(\mathbf{k}) = \mathbf{R}(\mathbf{k}) \mathbf{u}(\mathbf{k}). \quad (\text{A4})$$

Substituting this into the potential energy expression,

$$V = \frac{1}{2} \mathbf{u}^T R^T K R \mathbf{u}, \quad (\text{A5})$$

and using the expansion (A1), we obtain

$$V = \frac{1}{2} \sum_{\mathbf{k}} \mathbf{u}^{\dagger}(\mathbf{k}) \mathbf{R}^{\dagger}(\mathbf{k}) K \mathbf{R}(\mathbf{k}) \mathbf{u}(\mathbf{k}), \quad (\text{A6})$$

where K is the diagonal matrix of constraint spring constants and \dagger denotes Hermitian conjugation.

This motivates the definition of the mass weighted dynamical matrix,

$$\mathbf{D}(\mathbf{k}) = M^{-1/2} \mathbf{R}^{\dagger}(\mathbf{k}) K \mathbf{R}(\mathbf{k}) M^{-1/2}, \quad (\text{A7})$$

where M is the diagonal mass matrix. The phonon modes follow from the eigenvalue equation

$$\mathbf{D}(\mathbf{k}) \mathbf{u}(\mathbf{k}) = \omega^2(\mathbf{k}) \mathbf{u}(\mathbf{k}), \quad (\text{A8})$$

with $\omega^2(\mathbf{k})$ the eigenvalues corresponding to the squared angular frequencies of the phonon modes.

Appendix B: Code and Data Availability

All computational scripts and input files used in this work are openly available at:

<https://github.com/coentropy/MOFs>

Structures with CIF sizes above 35 kB were excluded to avoid memory bottlenecks. Neighbor environments were identified using `CrystalNN`[22] with a search cutoff of 25 Å. For the main dataset we used the default, chemically aligned settings with `x_diff_weight = 1.5`, which produce coordination numbers consistent with known metal and linker environments. For the UiO-66 tuning in Fig. 4, we instead reran `CrystalNN` with chemical heuristics effectively turned off (`distance_cutoffs = None`, `weighted_cn = True`, `x_diff_weight = 0`) and then retained only neighbors with `weight ≥ τ`. In this case the network is controlled purely by geometry through the τ filter: bonds and angles present in both the default and τ filtered networks are treated as primary UFF4MOF constraints, while those that appear only in the τ filtered network are interpreted as auxiliary long range constraints and assigned uniform spring constants (see the repository for specific values). The Maxwell–Calladine index was consistently evaluated at the Γ -point, while phonon dispersions were sampled along Setyawan Curtarolo [25] high-symmetry paths using 100 evenly spaced points per segment.

To validate the consistency between the UFF4MOF equilibrium bond distances and the geometric bond lengths extracted from the MOF structures, we compared the summed UFF radii r_{ij} against the actual interatomic separations obtained from the crystallographic coordinates. (Note: in the UFF expression $r_{ij} = r_i + r_j + r_{bo} + r_{en}$, r_{bo} and r_{en} are the bond-order and electronegativity corrections; here we set them to zero since their contributions are small for the bonds considered.) Across all linear bonds in the dataset, we found that the UFF equilibrium distances are systematically larger than the geometric bond lengths by approximately 5–7% on average. This suggests that the UFF radii modestly overestimate the bond lengths present in the structures, but remain within a relatively narrow range, so we adopt them as rest lengths in the rigidity model for the present, approximate treatment.

Appendix C: Silicon Benchmark

Since our present implementation builds the rigidity matrix from an explicit real-space reference cell containing a complete set of distinct bond and angle constraints, we compute the phonon dispersion of silicon using the standard eight atom conventional cubic cell rather than the two atom primitive cell. The comparison in Fig. 6 highlights several important features. The overall frequency range predicted by the rigidity model is higher than in the DFT reference calculation, reflecting the stiffer effective force constants in the harmonic spring

network. Along the $\Gamma \rightarrow X$ path, however, the dispersions are in close agreement, with comparable band shapes and similar degeneracies at the high-symmetry points. Along the $X \rightarrow K$ path the two spectra begin to diverge, yet the qualitative structure is still preserved. The most noticeable differences appear along the $\Gamma \rightarrow L$ path, where the relative ordering and spacing of branches do not fully align with the DFT results. Despite these discrepancies, the simplified rigidity-based model reproduces the principal features of the silicon phonon dispersion with reasonable accuracy. This agreement supports the use of the approach for capturing the dominant degree of freedom structure in more complex materials.

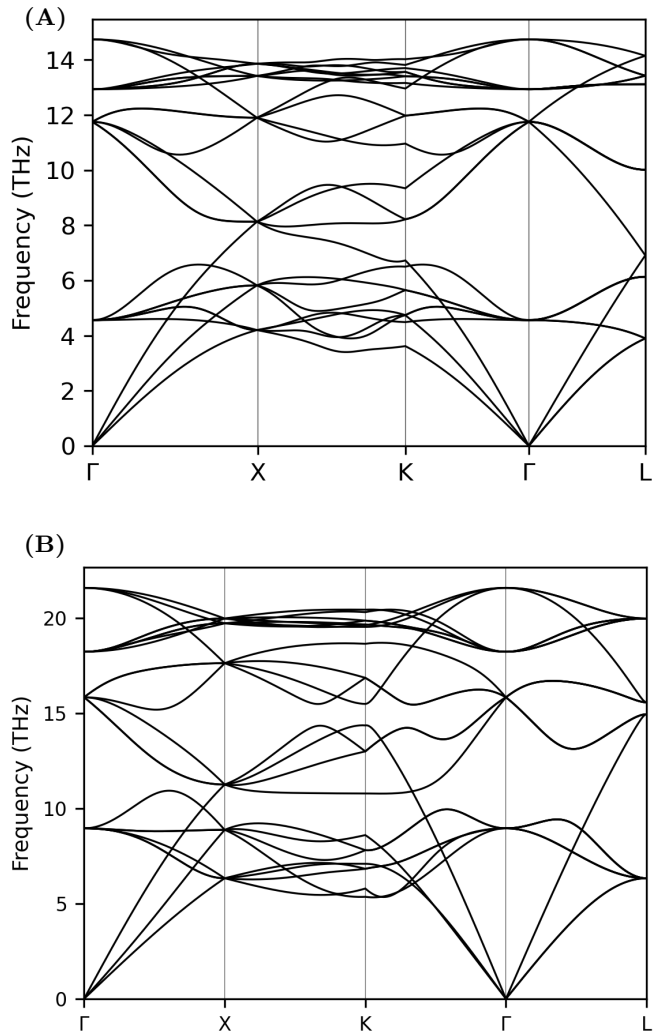


FIG. 6. (A) Phonon dispersion of a silicon conventional cell calculated by DFT in Quantum Espresso, and (B) the corresponding result from our rigidity-based model. The high-symmetry points coincide, and the overall branch shape is reproduced accurately. Frequencies from the rigidity model are slightly higher, reflecting its stiffer effective force constants relative to the ab initio calculation.

-
- [1] H. Furukawa, K. Cordova, M. O’Keeffe, and O. Yaghi, *Science (New York, N.Y.)* **341**, 1230444 (2013).
- [2] *Chemical Reviews* **112**, 673 (2012), pMID: 22280456, <https://doi.org/10.1021/cr300014x>.
- [3] L. R. Redfern and O. K. Farha, *Chem. Sci.* **10**, 10666 (2019).
- [4] F. zohra Zeggai, Z. Ait-Touchente, K. Bachari, and A. Elaissari, *Chemical Physics Impact* **10**, 100864 (2025).
- [5] N. C. Burtch, J. Heinen, T. D. Bennett, D. Dubbeldam, and M. D. Allendorf, *Advanced Materials* **30**, 1704124.
- [6] S. M. Moosavi, P. G. Boyd, L. Sarkisov, and B. Smit, *ACS Central Science* **4**, 832 (2018).
- [7] L. Sarkisov, R. L. Martin, M. Haranczyk, and B. Smit, *Journal of the American Chemical Society* **136**, 2228 (2014), pMID: 24460112.
- [8] A. Marmier and K. E. Evans, *Dalton Trans.* **45**, 4360 (2016).
- [9] R. J. Maurer, C. Freysoldt, A. M. Reilly, J. G. Brandenburg, O. T. Hofmann, T. Björkman, S. Lebègue, and A. Tkatchenko, *Annual Review of Materials Research* **49**, 1 (2019).
- [10] P. Z. Moghadam, S. M. J. Rogge, A. Li, C.-M. Chow, J. Wieme, N. Moharrami, M. Aragoñes-Anglada, G. Conduit, D. A. Gomez-Gualdrón, V. Van Speybroeck, and D. Fairen-Jimenez, *Matter* **1**, 219 (2019).
- [11] C. Cleeton and L. Sarkisov, *Nature Communications* **16**, 4806 (2025).
- [12] J. Park, H. Kim, Y. Kang, Y. Lim, and J. Kim, *JACS Au* **4**, 3727 (2024), <https://doi.org/10.1021/jacsau.4c00618>.
- [13] M. F. Thorpe, *Journal of Non-Crystalline Solids* **57**, 355 (1983).
- [14] D. J. Jacobs and M. F. Thorpe, *Phys. Rev. Lett.* **75**, 4051 (1995).
- [15] J. C. Maxwell, *The London, Edinburgh, and Dublin Philosophical Magazine and Journal of Science* **27**, 294 (1864).
- [16] C. R. Calladine, *International Journal of Solids and Structures* **14**, 161 (1978).
- [17] A. K. Rappe, C. J. Casewit, K. S. Colwell, W. A. G. III, and W. M. Skiff, *Journal of the American Chemical Society* **114**, 10024 (1992).
- [18] M. A. Addicoat, N. Vankova, I. F. Akter, and T. Heine, *Journal of Chemical Theory and Computation* **10**, 880 (2014).
- [19] D. E. Coupry, M. A. Addicoat, and T. Heine, *Journal of Chemical Theory and Computation* **12**, 5215 (2016), pMID: 27580382, <https://doi.org/10.1021/acs.jctc.6b00664>.
- [20] O. G. Chung, E. Haldoupis, B. J. Bucior, M. Haranczyk, S. Lee, K. D. Vogiatzis, S. Ling, M. Milisavljevic, H. Zhang, J. S. Camp, B. Slater, J. I. Siepmann, D. S. Sholl, and R. Q. Snurr, *Computation-ready experimental metal-organic framework (core mof) 2019 dataset*, <https://doi.org/10.5281/zenodo.14184621> (2024).
- [21] V. F. Yusuf, N. I. Malek, and S. K. Kailasa, *ACS Omega* **7**, 44507 (2022).
- [22] H. Pan, A. M. Ganose, M. Horton, M. Aykol, K. A. Persson, N. E. R. Zimmermann, and A. Jain, *Inorganic Chemistry* **60**, 1590 (2021), pMID: 33417450.
- [23] J. W. Rocks and P. Mehta, *Integrating local energetics into maxwell-calladine constraint counting to design mechanical metamaterials* (2024), arXiv:2208.07419 [cond-mat.soft].
- [24] S. P. Ong, W. D. Richards, A. Jain, G. Hautier, M. Kocher, S. Cholia, D. Gunter, V. L. Chevrier, K. A. Persson, and G. Ceder, *Computational Materials Science* **68**, 10.1016/j.commatsci.2012.10.028 (2012).
- [25] W. Setyawan and S. Curtarolo, *Computational Materials Science* **49**, 299–312 (2010).
- [26] S. R. Hall, F. H. Allen, and I. D. Brown, *Acta Crystallographica Section A* **47**, 655 (1991).
- [27] M. Islamov, P. Boone, H. Babaei, A. J. H. McGaughey, and C. E. Wilmer, *Chem. Sci.* **14**, 6592 (2023).
- [28] J. Winarta, B. Shan, S. M. McIntyre, L. Ye, C. Wang, J. Liu, and B. Mu, *Crystal Growth & Design* **20**, 1347 (2020), <https://doi.org/10.1021/acs.cgd.9b00955>.
- [29] H. Wu, T. Yildirim, and W. Zhou, *The Journal of Physical Chemistry Letters* **4**, 925 (2013), pMID: 26291357, <https://doi.org/10.1021/jz4002345>.
- [30] C. L. Kane and T. C. Lubensky, *Nature Physics* **10**, 39–45 (2013).